Powder Technology 470 (2026) 122053

Contents lists available at ScienceDirect

Powder Technology

journal homepage: www.journals.elsevier.com/powder-technology

Powder particle size and surface modification effects on aluminum-filled lattice structures in additive manufacturing of energetic materials

Carlo Rontini, Federico Giambelli, Christian Paravan *

Department of Aerospace Science and Technology, Politecnico di Milano, 34 via La Masa, I-20156, Milan, Italy

GRAPHICAL ABSTRACT

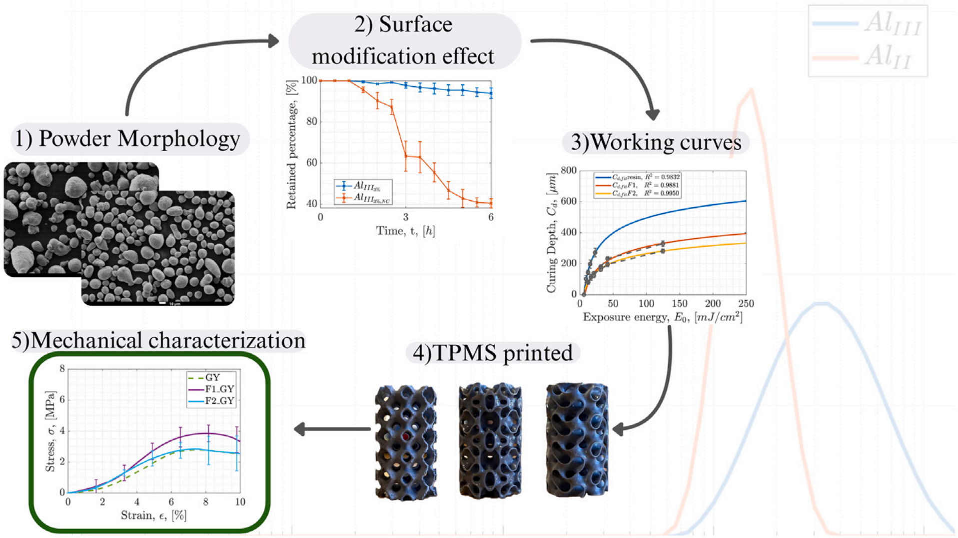

HIGHLIGHTS

- Micro-Al-filled resins (9.9 vol.%) were DLP printed as TPMS lattices (10% infill).
- Surface modification and PSD influenced sedimentation and printability.
- Resins loaded with broader PSD Al (F1) improved mechanical performance.
- F1-printed gyroids: +30% in yield strength, +10% in ductility over the baseline.
- F2 (finer, narrower PSD Al): higher print stability & reduced sedimentation than F1.

ARTICLE INFO

Keywords:
Triply periodic minimal surfaces
Digital light processing
Particle size influence
Powder surface modification

ABSTRACT

The incorporation of metallic fillers into photocurable resins offers a promising route for the fabrication of advanced energetic materials by Digital Light Processing (DLP). This study investigates the printability and compressive performance of triply periodic minimal surface (TPMS) lattice structures manufactured with micron-sized aluminum filled resins with 20 wt% loading (9.9 vol.%). Two micron-sized aluminum powders

---

* Corresponding author.
E-mail address: christian.paravan@polimi.it (C. Paravan).

https://doi.org/10.1016/j.powtec.2025.122053
Received 10 October 2025; Received in revised form 27 November 2025; Accepted 19 December 2025

Aluminum powder
Energetic materials

with distinct particle size distributions were evaluated to assess their influence on suspension stability, curing behavior and mechanical performance. Formulations were characterized through sedimentation over time, working curve analysis and filler content via density measurements and thermogravimetric analysis. Results indicate that suspension homogeneity is significantly improved via powder surface modification and optimized dispersant concentration. Broader particle size distribution promoted enhanced particle packing and reduced light scattering, resulting in increased curing depth with respect to the finer formulation. Compression testing (ASTM D695) revealed significant improvements in mechanical properties across all TPMS configurations. In particular, the Gyroid lattice exhibited a 30% increase in yield strength and a 10% increase in ductility with respect to the unfilled baseline. These findings confirm the suitability of aluminum loaded resins for high resolution DLP printing of functional lattice structures and emphasize the critical role of powder formulation in governing both print fidelity and mechanical response.

1. Introduction

The incorporation of solid powders into liquid suspensions is a cornerstone of powder technology, with direct implications for additive manufacturing (AM). In Vat Photo-Polymerization (VPP), particularly Digital Light Processing (DLP), the powder dispersion and sedimentation, and the light interactions with solid particles govern suspension stability, curing behavior, and the quality of printed parts [1–3]. Understanding how particle size distribution (PSD) and surface treatments influence these mechanisms is therefore critical to advancing solid loading photopolymer systems. DLP has emerged as a successful technique for the fabrication of cellular structures, offering excellent resolution, making it suitable for producing functional triply periodic minimal surface (TPMS) lattices [4–7]. Furthermore, DLP is widely used in applications involving resins loaded with functional fillers [8–11]. When considering aerospace engineering and advanced space mission exploration, DLP adaptability to high solid-loading systems makes it a promising candidate for future in-situ resource utilization (ISRU) scenarios [12–15].

Additive manufacturing (AM) offers disruptive opportunities for the fabrication of energetic materials (EM) in the development of solid and hybrid rocket fuels [16]. In this context, DLP has been employed to produce small-scale solid fuel elements with simple geometries. Nevertheless, most of these studies rely on inert resin matrices and typically exclude energetic fillers or utilize low filler loading [17–19]. Direct ink writing (DIW) has been used to manufacture solid fuel cylindrical grains containing aluminum as an energetic filler; however, printing at high solid loadings (20 wt%) was unsuccessful and the resulting parts exhibited low resolution [20]. In hybrid rocket propulsion, 3D-printing methods enable the manufacturing of solid fuel grains at small to intermediate scales. The integration of cellular structures in heterogeneous paraffin formulations resulted in the development of the armored grain concept [21,22], where a printed structure supports a liquefying fuel, enhancing both mechanical and ballistic performance. In these studies cellular structures embedded into a paraffin matrix introduced a ductile behavior to the solid fuel, making it more suitable for real application.

To expand the functionality of 3D-printed structures, metal powders can be incorporated into photocurable resins, improving mechanical properties and increasing energy content, fulfilling both structural and reactivity/combustion roles. The incorporation of metal particles into resin systems implies considerable problems for DLP procedures, such as increased light scattering, sedimentation, and cure inhibition [23]. Metal particles have been explored in DLP systems; however, these studies were limited to metal alloys processed with high-end, industrial 3D printers [24–26]. The impact of filler particle size and distribution on printability and structural performance is an important area of research. Larger particles can intensify sedimentation and diminish cure depth, whereas nanoscale particles influence rheology, resin homogeneity and increase light scattering [27]. These effects are particularly critical in the context of periodic lattice systems, where dimensional precision and interlayer adhesion play an important role for sustaining mechanical performance. Systematic studies investigating printability, stability, and mechanical behavior of energetic particle-loaded resins in DLP are still limited.

This work presents a study on the fabrication of aluminum-filled photopolymer lattice structures via DLP using a 20 wt% (9.9 vol.%) loading, specifically targeting their application as energetic reinforcements in solid propellant formulations. The solid loading was set to 20 wt% because this value is typical in solid fuel formulations [28]. Two microscale Aluminum (Al) powders were considered due to their high active aluminum content (C_{Al}) (in turn implying high energy content). Two PSDs are analyzed to understand their influence on printability and mechanical characterization. This study consists of two phases: (i) pre-printing and (ii) post-printing analysis.

The initial phase of the study focuses on printability, evaluating the influence of aluminum particle size on key parameters such as sedimentation stability, rheology characterization, and photopolymerization performance. Sedimentation studies were performed to examine the effects of PSD, powder surface modification, and dispersant concentration on suspension stability. Rheology characterization has been performed to understand mass loading. An analysis of the working curve was conducted to assess the impact of aluminum fillers on curing behavior, particularly the cure depth (C_d) and penetration depth (D_p). The mechanical characterization of the 3D-printed TPMS lattice structures focuses on the compressive behavior of three distinct architectures, each designed with a nominal infill (i) of 10%. TPMS were fabricated and evaluated under compressive loading conditions in accordance with ASTM D695. These structures were assessed to determine their suitability as reinforcement frameworks for integration into paraffin-based hybrid fuel systems. Furthermore, measurements of aluminum concentration were conducted to assess both localized and overall distribution of the filler within the printed structures.

This work introduces, for the first time, the successful incorporation of metallic powders into a low-cost DLP AM and demonstrating the feasibility of printing aluminum-loaded lattice structures with high geometrical resolution and mechanical integrity. These results establish a methodological foundation for energetic additive manufacturing, a rapidly emerging field. Beyond energetic systems, the findings provide transferable insights into how particle size distribution and surface modification govern suspension stability, curing behavior, and mechanical properties in metal-filled photopolymers.

2. Experimental section

This section outlines the materials used, the preparation of aluminum-filled photopolymer suspensions, and the experimental procedures used to evaluate stability, printability, and mechanical performance. Two micron-sized aluminum powders were investigated (Al_{III}, and Al_{II}). A detailed characterization of the powders has been provided. Relevant powder parameters (except for C_{Al}) and PSD were determined by laser granulometry (Malvern Mastersizer 2000), while powder morphology was examined with scanning electron microscopy (SEM, model : Hitachi TM3000). The C_{Al} in the powder was determined by a volumetric method based on H_2 release from $\mathrm{Al} + H_2O$ reaction [29,30]. A concise overview of the resin and dispersant is provided, followed by detailed descriptions of suspension preparation,

Table 1
Relevant parameters of the tested powders (Malvern Mastersizer 2000, dry dispersion).

ID	S_{sp} [m^2/g]	$d_{3,2}$ [µm]	$d_{4,3}$ [µm]	$d_{0.1}$ [µm]	$d_{0.5}$ [µm]	$d_{0.9}$ [µm]	C_{Al} [%]	$\frac{\Delta d}{d}$ [–]
Al_{III}	0.20	29.9	41.2	16.5	35.1	74.8	99.1 ± 0.2	1.66
Al_{II}	0.40	15.0	16.5	10.6	15.7	23.4	99.5 ± 0.4	0.82

and characterization methods. Rheology characterization of the slurry was performed with a rheometer (MCR502, Anton Paar). Subsequently, the printing strategies adopted for TPMS manufacturing are presented, and the post-printing analysis procedures are introduced. An estimation of localized aluminum concentration and an evaluation of sedimentation effects during printing was performed by TGA Netzsch STA 449 F5 Jupiter system at an heating rate of 10 K/min in Ar. Uniaxial compression tests were performed using an MTS 858 Mini Bionix II testing system.

2.1. Metal powders

Air-passivated micron-sized aluminum powders were considered in the study. They have nominal sizes of 30 and 15 µm (Al_{III}, and Al_{II} respectively), and are produced by AMG Alpoco (UK) with purity ≥98%. All particle diameters ($d_{0.1}$, $d_{0.5}$, and $d_{0.9}$) are expressed in volume percentage. The tested powders and their relevant size data are presented in Table 1.

Span number is defined as:

$$\frac{\Delta d}{d} = \frac{d_{0.9} - d_{0.1}}{d_{0.5}} \tag{1}$$

A small span value ($\frac{\Delta d}{d} < 1$) indicates a narrow and homogeneous PSD, whereas a large span value ($\frac{\Delta d}{d} > 1.5$) denotes a broad and heterogeneous distribution. Micron-sized powders feature specific surface area (S_{sp}) values < 0.5 m^2/g, as determined by laser granulometry, yielding high mean particle diameter, as confirmed by the volume-weighted mean diameter ($d_{4,3}$) and surface-based mean diameter ($d_{3,2}$). The Al_{III} powder exhibits a broad particle size distribution, as indicated by its 10th and 90th percentile ($d_{0.1}$ and $d_{0.9}$ respectively) particle diameters and by $\frac{\Delta d}{d}$ (see Table 1). The median particle diameter ($d_{0.5}$) is approximately 35 µm, slightly deviating from the nominal particle size. On the other hand, Al_{II} has a narrower particle size distribution than Al_{III}. Al_{II} exhibits $d_{0.1}$ and $d_{0.9}$ particle diameters close to each other, as indicated also from a small $\frac{\Delta d}{d}$. The median particle diameter ($d_{0.5}$) is very similar to nominal particle size specification. PSD is shown in Fig. 1, where the broader particle size distribution of Al_{III} is evident, with particle diameters ranging from 7.6 µm to 120.2 µm. Particle morphology shows mainly spherical particles for both powders, with few irregularly shaped (yet rounded) particles with exotic shapes. A smooth texture is common to the two powders. Both powders exhibit $C_{\text{Al}} > 98\%$, which is typical of spherical, air-passivated micron-sized Al powders. A higher C_{Al} corresponds to enhanced energy content and improved combustion performance. Such powders are generally resistant to oxidation and aging phenomena [31]. Both Al powders feature a thin Al_2O_3 layer on their surface.

2.2. Formulation

A general purpose commercial clear ABS-Like Resin Pro 2 UV resin (365 ÷ 405 nm reticulation wavelength) for SLA/DLP was acquired from Shenzhen Anycubic Technology Co. (China) and used as received. It has been selected because of its mechanical properties that resemble those of ABS and because of its short curing time. This material demonstrates superior flexibility relative to other commercial resins in tensile tests [32].

BYK-111 from BYK Chemie Gmbh (Germany), a non-ionic dispersant, was chosen for suspension tailoring. The selection of this dispersant is based on its effective performance in suspending solid particles within resin for DLP applications [1,33–35].

A Photon Mono X2 3D printer from Shenzhen Anycubic Technology Co. (China) was used for DLP 3D printing process.

2.2.1. Suspension preparation

The very first step involved the pure mixing of resin with Al powder. However, the resulting slurry was highly unstable and sedimented rapidly over time. Consequently, the dispersant was employed. Two different suspension preparation methods were employed for micron-sized aluminum powders: non-surface modified and surface modified procedure. The preparation of non-surface modified aluminum-filled resin suspensions followed a multi step mixing protocol. Initially, the desired amount of resin was added to a beaker, followed by the specified quantity of dispersant. The mixture was stirred for 30 min to ensure homogeneity. Aluminum powder was then incorporated in 5 g incrementing steps, with 30 min of stirring after each addition, until the full targeted mass was reached. This staged addition strategy was adopted to mitigate viscosity build-up during mixing and to improve particle dispersion [36].

The surface modified powder preparation followed the procedure similar to the one described by Stefan et al. [37]. A mixture consisting of 45 wt.% isopropyl alcohol (IPA) and 55 wt.% Al powder was prepared in a beaker. Dispersant was added at a concentration proportional to the powder mass (in the range 1 to 5 wt.%). To guarantee complete spread of the dispersant over the particles, the mixture was stirred for 30 min with an electric stirrer. Subsequently, the suspension was placed in an oven at 333 K for a minimum of 12 h to ensure complete evaporation of the IPA. After drying, the solid residue was weighed to confirm total solvent removal. The dried, surface modified powder was then incorporated into the resin and mixed for 1 h to form the final printable suspension. The effectiveness of the powder surface modification is assessed employing a C_{Al} test on the pristine and the surface modified powder. The suspension was prepared under ambient atmospheric conditions in a closed, dry environment. Under these conditions, oxidation or aging effects were negligible [31], and the powder can be considered to have preserved its original quality.

2.2.2. Suspension characterization

To achieve a homogeneous slurry containing solid particles, the use of a dispersant is essential. An optimal amount of dispersant leads to low compound viscosity, stable dispersion, high printing precision, and smooth printed surfaces. Insufficient or excessive dispersant causes issues such as poor flow, instability, low precision, and rough surfaces. To determine the ideal concentration, two different analytical methods have been employed: rheological analysis to evaluate slurry viscosity and sedimentation tests to observe particle stability over time [1,3]. The photopolymerization performance of the slurries and the quality of the printed parts are strongly governed by their rheological properties, with viscosity and dispersion stability being key indicators [2,34,38,39]. Suspension stability was assessed through sedimentation over time measurements and rheological characterization was employed to understand the loading effects on the viscosity and therefore on printability. Stability of the slurry was evaluated from the sedimentation tests. Sedimentation tests were conducted by measuring the height of the sedimented solid particles every 30 min for 6 h and then after 24 and 48 h as illustrated in Fig. 2. The typical printing time was approximately 3 h; therefore, a measurement window of 6 h was selected to capture the sedimentation behavior during printing. Additionally, two further measurements at 24 h and 48 h were performed to assess sedimentation over an extended timescale. The powder retained percentage ($R_{\%}$) is measured with the following equation:

$$R_{\%} = \frac{H_0 - H_{sed}}{H_0} \tag{2}$$

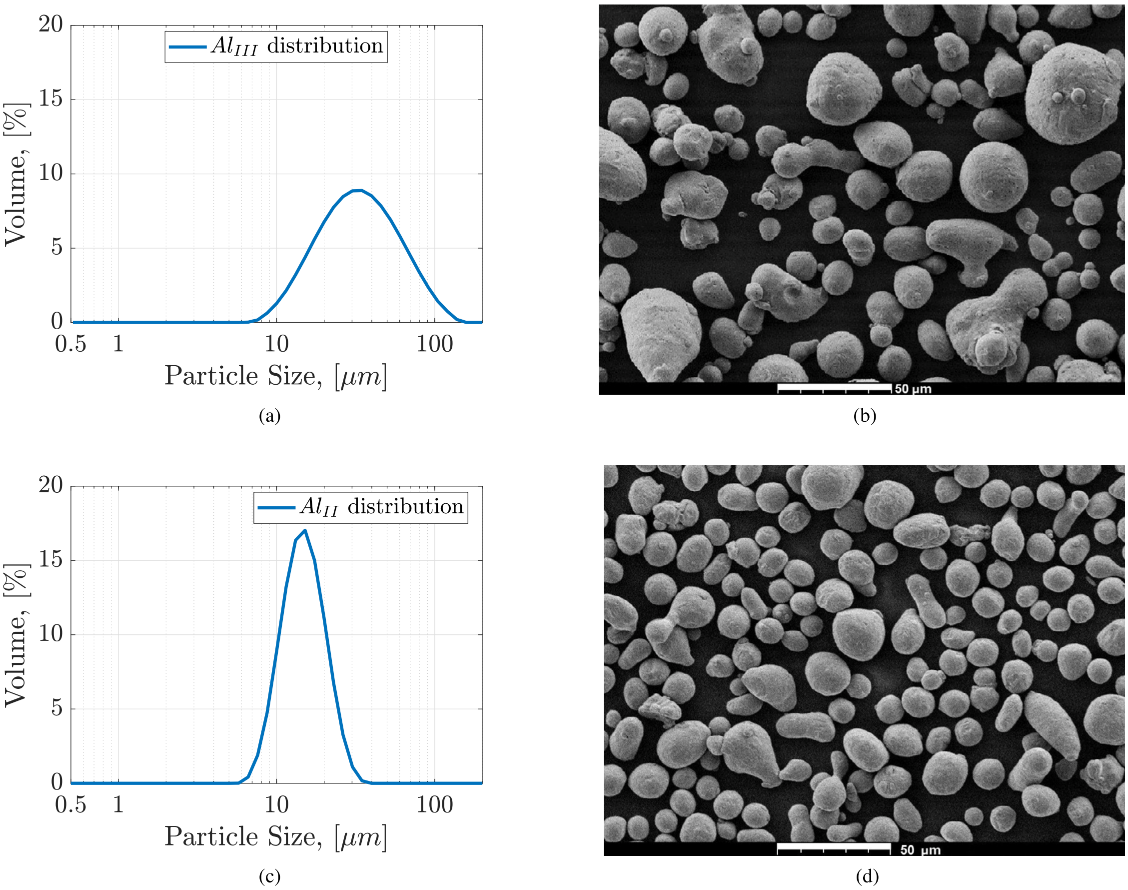

(a) (b) (c) (d)

Fig. 1. PSD and SEM images of the tested powders: (a) PSD of Al_{III}, (b) SEM of Al_{III}, (c) PSD of Al_{II}, and (d) SEM of Al_{II}.

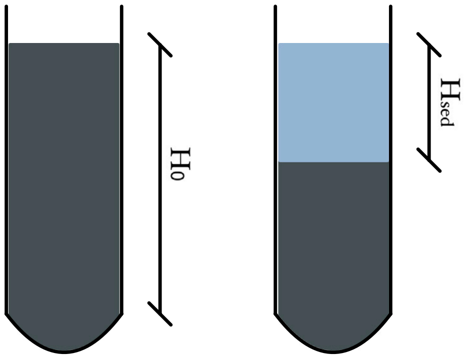

Fig. 2. Homogeneous suspension and sedimented suspension (Image is not to scale).

where H_0 is the initial height of the slurry inside the test tubes and H_{sed} is the height of non-homogeneous slurry as illustrated in Fig. 2. Three samples for each formulation are tested to ensure repeatability.

The viscosities of the unloaded and loaded resins were experimentally determined over a shear rate ($\dot{\gamma}$) range from 1 ÷ 100 s^{-1}, in order to characterize the printability of the formulations. The acceptable upper limit of viscosity found in literature is in the range of 3 Pa s at $\dot{\gamma}$ of 10 ÷ 100 s^{-1} [2,40,41].

2.3. Printing

2.3.1. Working curves

The photopolymerization ability of the suspension is a critical factor for DLP 3D printing, which depends on the composite parameters of the slurry, including the proportion and type of metal powder, the particle size, and the properties of photosensitive resin [42–45]. Therefore, obtaining correct working curves for loaded resin is crucial to achieve a good overall printing process.

The C_d is defined as the depth at which light energy is enough to induce the resin to reach the gel point [23]. The resin attains the gel point when the light energy exceeds critical energy (E_c); otherwise, it stays in a liquid state. The C_d is determined using Jacob's formulation of the Beer–Lambert law [42]:

$$C_d = D_p \ \ln\left(\frac{E_0}{E_c}\right) \tag{3}$$

where E_0 represents the UV exposure energy and D_p represents the penetration depth. The photocuring behavior is delineated by plotting C_d against $\ln(E_0)$ on a semi-logarithmic plot. The outcome is a graph referred to as the working curve, from which D_p and E_c may be derived. D_p is the slope of the line in such a graph, whereas E_c is the intercept with the X-axis. Both D_p and E_c are solely resin parameters and are unaffected by exposure. Consequently, both the slope and intercept of the operational curve are unaffected by the technical parameters. Solid particles contained in photocurable resins substantially interfere with the photopolymerization process due to light absorption and scattering. Scattering is an optical phenomenon when the direction of light alters due to the presence of irregularities in the medium. The primary distinction between solid filled resins and the unloaded counterparts resins is in the scattering of the forward beam, which redirects a portion of the UV energy from its original trajectory. Consequently, both light scattering and absorption diminish the energy intensity of light passing through the resin medium containing distributed solid particles. The C_d of these resins may be described by the following equation [23]:

$$C_d = \frac{2}{3} \cdot \frac{d_{0.5}}{\phi \ \beta \ \Delta n^2} \ln\left(\frac{E_0}{E_c}\right) \tag{4}$$

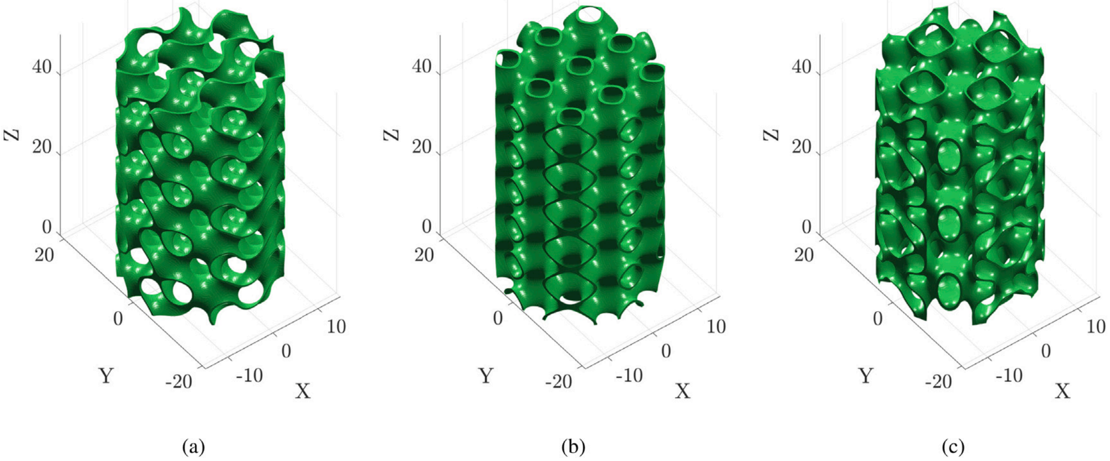

Fig. 3. TPMS representation: (a) GY, (b) SP, and (c) F-RD. These geometries differ in S/V and curvature distribution, influencing both printability and mechanical response.

where $d_{0.5}$ is the median particle size diameter, ϕ is volume fraction of solid particles, β is a parameter including particle size and beam wavelength and Δn^2 is the refractive index (RI) contrast, which is the difference between the RIs of the suspended solid particles and the photo-curable matrix [23]. Typical values for the RIs of the materials of interest are (i) 1.47-1.55 for the plain resin [23], (ii) 1.37 for the Al [46], (iii) 1.70-1.77 for Al_2O_3 [23]. The C_d dependence on Δn^2 shows the faint (if of any significance) impact of RI differences between Al and Al_2O_3.

The working curves of aluminum-loaded resins were obtained following a standardized photopolymerization protocol. The average UV power output of the DLP printer was first measured using a calibrated UV meter obtained from Shenzhen CBD Technology Co., Ltd (China). Aluminum-filled resin droplets were dispensed onto a transparent film and photopolymerized for different exposure times. After the uncured resin was removed, the cured depth (C_d), the thickness of the cured layer, was measured using a micrometer. Each exposure dose was repeated three times to ensure measurement repeatability and accuracy. The C_d was plotted as a function of exposure energy to generate the working curve. Eq. (3) was used to determine D_p from C_d and $\ln(E_0/E_c)$. The required exposure energy for a target layer thickness (t_{layer}) was calculated using the empirical relation $t_{\text{layer}} = 0.5 \cdot C_d$, as previously established for filled systems to ensure proper interlayer adhesion [23]. The t_{layer} was set to be at least twice the $d_{3,2}$ of the solid filler. Corresponding exposure times were determined by dividing the required energy by the measured mean power output.

2.3.2. Geometry design

The printing process begins with a Matlab script designed to generate a standard tessellation language (STL) file. The sliced file was then transferred to the DLP printer for fabrication. Three different TPMS geometries are analyzed in this study: Gyroid, Schwarz Primitive, and F-Rhombic Dodecahedron. The selected geometries were chosen to provide different surface-to-volume ratios (S/V) and for their favorable mechanical properties compared to other TPMS structures. All TPMS lattice structures were fabricated with a nominal infill density of 10% and a wall thickness of 0.4 mm and they are shown in Fig. 3. Investigated TPMS are hereby presented in details. Mathematical descriptions of the cellular structures consider Cartesian coordinates (x, y, z), while unit cell size and infill are identified by L and i, respectively.

The Gyroid (GY) is an open cell structure that represents a TPMS first described by NASA scientist A. Schoen [47]. TPMS exhibit no joints or discontinuities, thereby effectively minimizing stress concentration effects. The GY surfaces are constructed by the spatial periodic repetition of unit cells. GY structures are described mathematically by the following equation [48]:

$$\sin\left(\frac{2\pi x}{L}\right)\cos\left(\frac{2\pi y}{L}\right)+\sin\left(\frac{2\pi y}{L}\right)\cos\left(\frac{2\pi z}{L}\right)+\sin\left(\frac{2\pi z}{L}\right)\cos\left(\frac{2\pi x}{L}\right)=0 \tag{5}$$

In actual GY a layer thickness t is associated with the surface to create the cellular solid. Due to its complicated geometry, the GY lattice is often made via additive manufacturing. Finite element analyses show that it has lower anisotropy than other TPMS structures [49]. Parenti et al. [50] examined the relationship between i, L and t_{layer} and, consequently, it is employed in the GY printing process. A suggested equation yields extremely good fitting (R^2=99.97%) for $5 < L < 50$ mm and $5\% < i < 50\%$. The proposed equation states:

$$t_{\text{layer}} = 0.371 \cdot L^{0.997} \cdot i^{1.051} \tag{6}$$

The Schwarz-Primitive (SP) surface is a TPMS that was first described by H. Schwarz [51]. Like other TPMS structures, the Schwarz P surface has no joints or discontinuities, which helps minimize stress concentration effects. The SP structure exhibits a compressive behavior comparable to that of the GY geometry and features the lowest S/V among TPMS geometries [52,53]. Mathematically, the SP surface can be described by the implicit equation:

$$\cos\left(\frac{2\pi x}{L}\right)+\cos\left(\frac{2\pi y}{L}\right)+\cos\left(\frac{2\pi z}{L}\right)=0 \tag{7}$$

The F-Rhombic Dodecahedron (F-RD) surface is a TPMS discovered by A. Schoen [47]. The F-RD has the same symmetries as a cubic close-packed assembly of congruent spheres and it has no self-intersections. The F-RD lattice shows enhanced energy absorption at low infill and the highest S/V ratio among TPMS structures [53,54]. Mathematically, the F-RD surface is described by:

$$\begin{aligned}&4\cos\left(\frac{2\pi x}{L}\right)\cos\left(\frac{2\pi y}{L}\right)\cos\left(\frac{2\pi z}{L}\right)+\\&-\cos\left(\frac{4\pi x}{L}\right)\cos\left(\frac{4\pi y}{L}\right)-\cos\left(\frac{4\pi x}{L}\right)\cos\left(\frac{4\pi z}{L}\right)+\\&-\cos\left(\frac{4\pi y}{L}\right)\cos\left(\frac{4\pi z}{L}\right)=0\end{aligned} \tag{8}$$

The GY structures were generated using Eq. (6), while for SP and F-RD geometries, cell sizes were determined based on geometric analogies with the cubic Bravais lattice system [55,56]. Specifically, the SP geometry corresponds to a simple cubic configuration, the GY to a body-centered cubic configuration, and the F-RD to a face-centered cubic configuration.

2.4. *Characterization of printed parts*

2.4.1. *Aluminum concentration*

Two complementary approaches were utilized to estimate the actual aluminum concentration: (i) density measurements and (ii) thermogravimetric analysis (TGA). Density measurements based on Archimedean method provide an estimation of the overall aluminum concentration in the printed structure. Thermogravimetry provides insights into localized Al content.

The overall aluminum mass fraction in the printed structures (w_{Al}) was determined using density measurements of both the pure resin and the aluminum-loaded composite material. The immersion medium was ethanol. For each TPMS geometry, three unloaded and three aluminum-loaded specimens were printed with longitudinal axis (Z in Fig. 3) parallel to the build plate. Specimen dimensions were selected to replicate the outer diameter and orientation of the ballistic specimens used for armored grain tests [21,22]. The density of the composite material, composed of a resin matrix and dispersed aluminum filler, was calculated using the inverse rule of mixtures, as:

$$\frac{1}{\rho_{\text{loaded}}} = \frac{w_{\text{resin}}}{\rho_{\text{resin}}} + \frac{w_{\text{Al}}}{\rho_{\text{Al}}} = \frac{1 - w_{\text{Al}}}{\rho_{\text{resin}}} + \frac{w_{\text{Al}}}{\rho_{\text{Al}}} \tag{9}$$

where ρ_{loaded} is the measured density of the aluminum-loaded resin, ρ_{resin} is the density of the pure resin, ρ_{Al} is the theoretical density of aluminum ($\rho_{\text{Al}} = 2700\ \text{kg/m}^3$), w_{resin} and w_{Al} are the respective mass fractions of resin and aluminum. This expression enables calculation of the overall aluminum mass fraction (w_{Al}) in the printed structure based on the measured composite density. Samples were extracted from the first and last printed layers, representing the initial and final stages of the build process. Three specimens were collected from each region to simulate the impact of particle sedimentation over time. Aluminum content was quantified based on the mass loss associated with resin pyrolysis, gasification, and thermal degradation. A baseline test was performed on pure resin to determine its residual mass ($m_{\text{resin, residual}}$) after complete decomposition. The aluminum mass fraction (w_{Al}) in each composite sample was calculated using the following relation:

$$w_{\text{Al}} = \frac{m_{\text{residual}} - m_{\text{resin, residual}}}{m_{\text{initial}}} \times 100 \tag{10}$$

where m_{residual} is the residual mass measured after thermal decomposition, and m_{initial} is the initial mass of the sample. This method enables estimation of localized aluminum content and provides insight into filler vertical distribution resulting from sedimentation during the DLP printing process.

2.4.2. *Mechanical characterization*

Uniaxial compression tests were performed accordingly to ASTM D695 standard. The specimens were cylindrical, with a height of 25.4 mm (1 inch) and a diameter of 12.7 mm (0.5 inch). Tests were conducted at room temperature (291 ± 3 K) under displacement control, using a constant crosshead speed of 1 mm/min. For each condition, a minimum of three specimens were tested, and the results were averaged with standard deviations reported.

These tests were conducted to evaluate the compressive behavior of three different TPMS structures, allowing for analysis of geometric influence on mechanical response. In addition, samples printed with different PSD were tested to assess the influence of this powder parameter on mechanical performance.

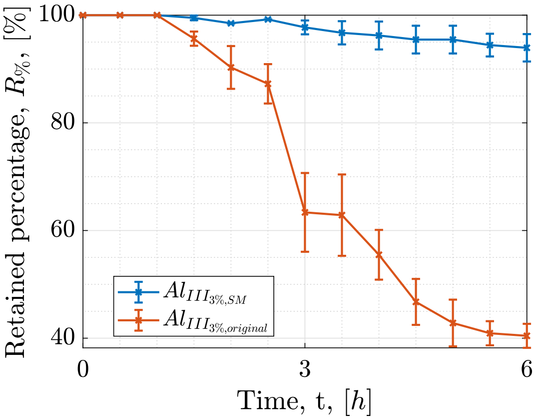

Fig. 4. Sedimentation history in time for Al_{III} with 3 wt.% dispersant: surface modified procedure contrasted with non-modified one.

3. Results and discussion

3.1. *Sedimentation over time*

In an earlier step, suitable dispersant mass fraction was determined by adding BYK-111 to the pristine resin, followed by gradual addition of Al powder (see Section 2.2.1). This process resulted in an unstable suspension; therefore, a modified procedure was implemented. Results for 3 wt.% dispersant concentration are reported in Fig. 4 (error bars represent the standard deviation across multiple measurements). The original formulation resulted in an unstable suspension over time, attributed to insufficient adhesion of the dispersant to the particles surface, which limited effective dispersion. Therefore, from now on, all the discussed formulations feature surface modifications.

The dispersant concentration plays a critical role in achieving a stable suspension with optimal printability and acceptable viscosity [3, 57]. Insufficient dispersant may lead to incomplete surface coverage of the particles, resulting in poor stabilization, whereas excessive dispersant can induce flocculation due to bridging effects. The influence of dispersant concentration on sedimentation behavior is clearly observed in Fig. 5 for Al_{III} loaded resin and in Fig. 6 for Al_{II} loaded resin. For the Al_{III} formulation, dispersant concentration testing began at 2 wt%, as this was the lowest concentration that demonstrated a measurable degree of stability over time. Among the tested formulations, the suspension containing 5 wt% dispersant exhibited the lowest stability over an observation window of 48 h. The latter formulation reduced data scattering in the first six hours, but afterward suspension stability dropped. The same trend is visible for Al_{II} formulation. This behavior is attributed to excessive dispersant, which promotes flocculation. Since the dispersant concentration is expressed as a percentage relative to the powder mass, the optimal concentration identified is expected to remain valid across varying solid loadings, assuming similar particle surface characteristics.

The sedimentation rate varied significantly with different particle sizes, with coarser particles exhibiting more rapid settling, as shown in Fig. 7. This behavior is primarily attributed to the relatively wide PSD span and large $d_{4,3}$ of Al_{III}, implying quite low S_{sp} (see Table 1). Thus, resin–particle interfacial interactions are reduced and sedimentation is promoted. It can be observed that, during the initial phase of the measurement, a higher level of data scattering is associated with Al_{III}. This behavior is attributed to the broader particle size distribution of the powder. Following the C_{Al} test procedure outlined in Section 2.1, the C_{Al} of the powder is determined to verify that the results of Fig. 4 can be attributed to dispersant deposition on powder surface. Five samples of $\text{Al}_{III,3\%}$ has been tested and two samples of pure Al_{III} are analyzed for reference. For the surface-modified powder ($\text{Al}_{III,3\%}$),

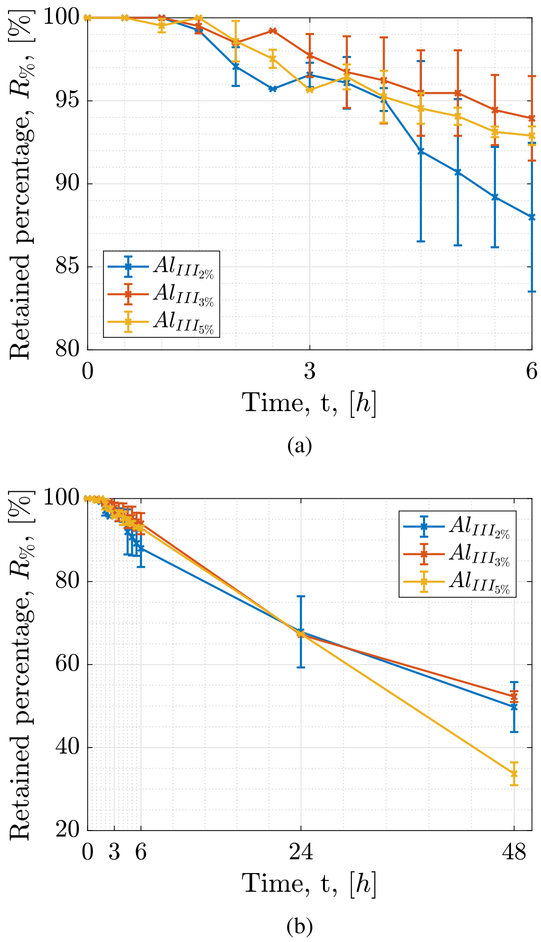

(a)

(b)

Fig. 5. Sedimentation history in time for Al_{III} (surface modified): dispersant concentration influence over (a) 6 h and (b) 48 h. Retained percentage is defined by Eq. (2).

Table 2
Summary of aluminum filled resin formulations used in this study (dispersant is 3 wt% of the powder mass).

ID	Resin [wt.%]	Al_{III} [wt.%]	Al_{II} [wt.%]	BYK-111 [wt.%]
F1	79.4	20	–	0.6
F2	79.4	–	20	0.6

prepared with 3 wt% dispersant relative to the powder mass, the measured C_{Al} was 93.6 ± 0.7%, whereas the pristine reference powder (Al_{III}) exhibited 99.1 ± 0.2%. The surface modified powder ($\mathrm{Al}_{III,3\%}$) was expected to show $C_{\mathrm{Al}} \approx 96\%$. The measured value of 93.6 ± 0.7% is deviating from the expected result, but taking into account potential variations in surface modification efficiency and measurement uncertainty results indicate an overall effective dispersant deposition on the powder surface. Based on the results of the sedimentation tests, the most stable and processable formulations were selected for further investigation. These formulations demonstrated superior dispersion stability, minimized sedimentation over time, and maintained suitable properties for DLP printing. The formulations used for printing the TPMS lattice structures identified as F1 and F2 are summarized in Table 2.

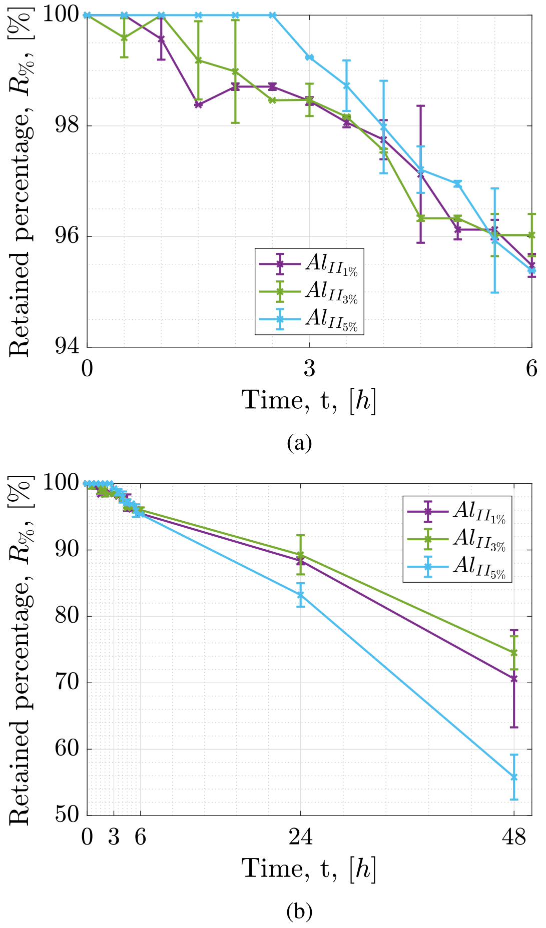

(a)

(b)

Fig. 6. Sedimentation history in time for Al_{II} (surface modified): dispersant concentration influence over (a) 6 h and (b) 48 h. Retained percentage is defined by Eq. (2).

3.2. Rheological characterization

The rheological characterization results are summarized in Fig. 8. Under the investigated conditions, all suspensions behaved as Newtonian fluids and remained below the upper limit of viscosity for printability. As shown in Fig. 8, adding powder to the resin increases viscosity. No significant difference is observed between formulations F1 and F2; however, F1, featuring a broader PSD, exhibits a slightly higher viscosity than F2 with its narrower PSD, a difference likely due to the more efficient particle packing in F1.

3.3. Working curves

Working curves of the aluminum-loaded resin formulations were obtained following the methodology described in Section 2.3.1 and they are visually presented in Fig. 9. The error bars represent the standard deviation across experimental measurements. The critical energy (E_c) corresponds to the point where the curves intersect the x-axis in Fig. 9. The plain resin ($E_c = 6.12\ \mathrm{mJ/cm^2}$) exhibits a higher printability, consistent with lack of solid fillers. Nevertheless, loaded formulations maintain E_c values below 10 $\mathrm{mJ/cm^2}$, confirming no potential issues with photopolymerization and overall good curing behavior. After obtaining the working curve parameters (C_d, E_c, and E_0) from Fig. 9, the corresponding D_p values for the tested formulations can be determined. Unloaded formulation has the highest printability among the three formulations. Fine formulation (F2) exhibits the lowest

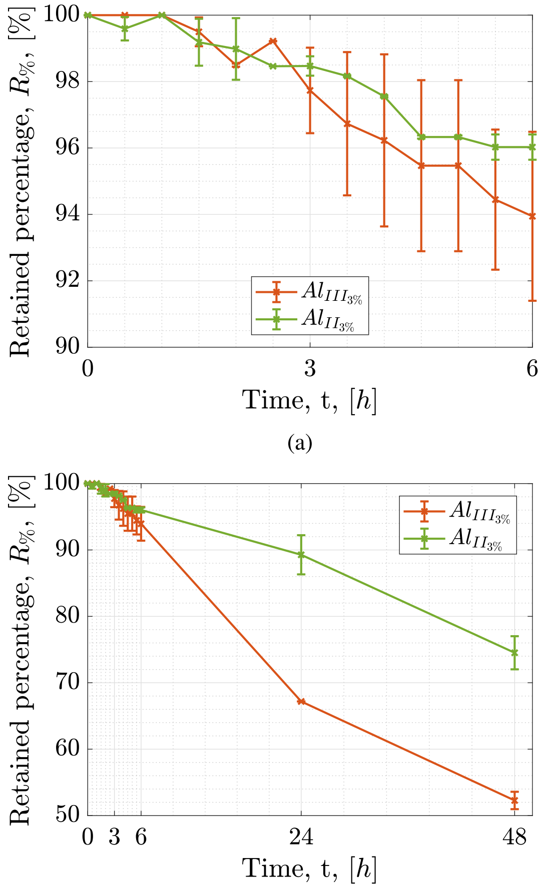

(a)

(b)

Fig. 7. Sedimentation history in time over (a) 6 h and (b) 48 h for Al_{III} and Al_{II} (surface modified) with best dispersant concentration to achieve maximum degree of stability.

curing behavior in the dataset, even if it shows no major curing issues, demonstrated by its D_p. Large particles scatter light at small angles relative to the beam, while smaller particles scatter light at larger angles. This increased scattering, particularly with smaller particles, hinders deep light penetration into the resin, thereby reducing the effective curing depth, as shown in Eq. (4). A similar trend is observed in Fig. 9, where the formulation containing finer particles (F2) exhibits increased light scattering, resulting in reduced C_d and D_p. This effect is the result of increased light scattering caused by the finer particle size distribution. A reduction in curing behavior can also be attributed to increased light absorption. This effect is linked to differences in specific surface area between the samples, as finer particles possess larger surface area, which enhances light absorption and consequently reduces the effective C_d [13].

Based on a measured mean power (P_{mean}) of 4.16 ±0.25 mW/cm^2, the corresponding printing parameters derived from working curves, are summarized in Table 3. The layer thickness was selected to be at least twice the $d_{3,2}$ of the powder used to ensure proper interlayer adhesion between resin and powder. All the structures were printed in a horizontal orientation to mitigate sedimentation effects during the printing process, while maintaining sufficient mechanical integrity [58]. Fig. 10 shows the three TPMS configurations, printed using the parameters summarized in Table 3.

3.4. Aluminum concentration

3.4.1. Overall aluminum concentration

The results of density measurements are summarized in Table 4.

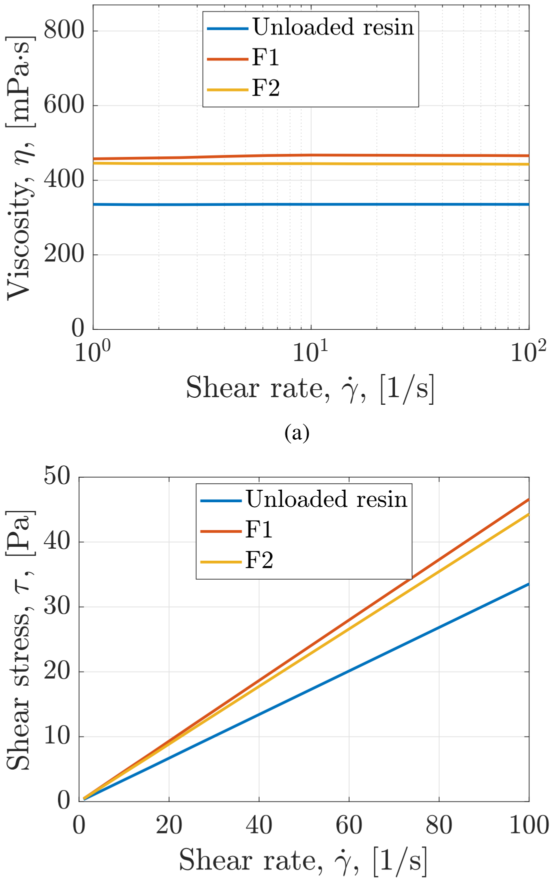

(a)

(b)

Fig. 8. The rheological characteristics of unloaded and loaded configurations: (a) viscosity as a function of shear rate and (b) shear stress as a function of shear rate.

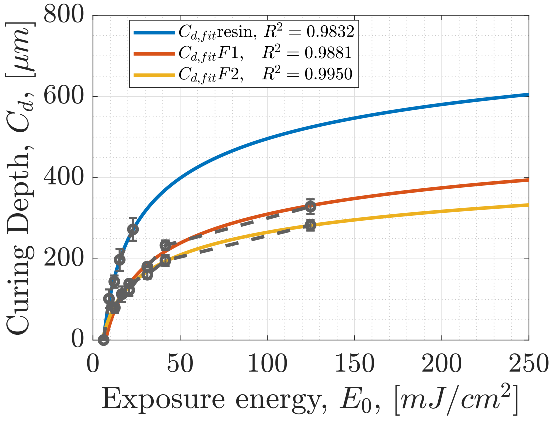

Fig. 9. Working curves for loaded and unloaded resins.

Table 3
Formulations printing parameters.

ID	t_{layer} [μm]	Building orientation [°]	E_0 [$\frac{mJ}{cm^2}$]	E_c [$\frac{mJ}{cm^2}$]	D_p [μm]
Plain Resin	50	0	10.00	6.12	35.20
F1	60	0	18.00	5.52	34.29
F2	50	0	16.00	7.28	31.21

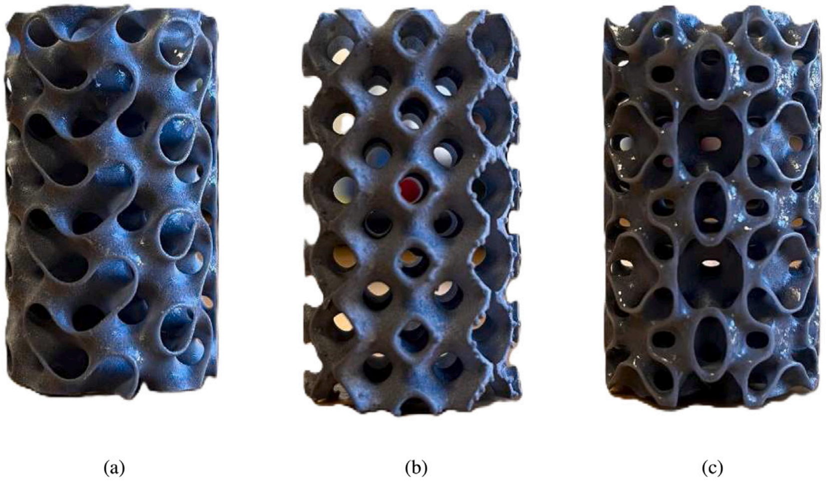
(a) (b) (c)

Fig. 10. TPMS structures printed: (a) F1_GY, (b) F1_SP, and (c) F1_ F-RD.

Table 4
Density measurements for TPMS.

Structure	ρ_{plain} [kg/m^3]	ρ_{loaded} [kg/m^3]	w_{Al} [%]
F1_GY	1183.8 ± 2.8	1353.7 ± 5.3	22.2 ± 0.6
F1_SP	1187.2 ± 4.7	1330.7 ± 9.3	19.4 ± 1.1
F1_F-RD	1186.6 ± 2.9	1321.1 ± 14.0	18.2 ± 1.7
F2_GY	1183.8 ± 2.8	1359.0 ± 9.4	23.0 ± 1.1

Table 5
Investigated printed structures: mechanical response under compression (ASTM D695, 1mm/min, 18 ± 3°).

Specimen	σ_y [MPa]	ϵ_y [%]	E [MPa]
GY	2.85 ± 0.17	6.92 ± 0.87	46.26 ± 11.04
SP	0.86 ± 0.2	7.01 ± 0.56	14.94 ± 3.59
F-RD	3.63 ± 0.37	5.65 ± 0.04	102.60 ± 4.58
F1_GY	3.84 ± 0.25	7.60 ± 0.47	78.40 ± 2.85
F1_SP	1.40 ± 0.15	8.20 ± 0.22	23.46 ± 2.96
F1_F-RD	4.24 ± 0.15	5.47 ± 0.92	114.51 ± 5.20
F2_GY	2.83 ± 0.29	7.08 ± 0.29	64.07 ± 8.11

The results indicate that the actual w_{Al} in the printed structures is approximately 20 wt%, with only minor variations observed across the different TPMS geometries. These differences may suggest that structural complexity and S/V influence the effective retention of aluminum during the printing process. Among the geometries tested, the F-RD structure, exhibiting the highest S/V, showed the lowest measured aluminum concentration. For the formulation containing smaller particles (F2), no significant issues associated with particle size were observed. The measured aluminum content showed good agreement with the theoretical mass loading of 20 wt%. Globally it can be noted that all TPMS, with broad and fine PSD, are uniform in aluminum distribution.

3.4.2. Localized aluminum concentration

In order to analyze the localized aluminum concentration a TGA has been performed. Three samples were extracted from the initial and final printed layers of the construction to replicate the impact of sedimentation over time. Mass loss, attributed to resin pyrolysis, allows for the precise calculation of Al powder content, as the residual mass of the resin was established via a baseline test ($m_{\text{resin, residual}} \approx$ 4.5%). The results of those tests are summarized in Fig. 11, where the *Top* position corresponds to the final layers printed and the *Bottom* position to the initial layers printed during the build process. TGAs are consistent with the sedimentation tests, confirming that coarser particles tend to settle more rapidly than finer ones. In contrast, finer particles exhibit greater suspension stability throughout the printing process. The average aluminum mass loading, calculated as the mean of the *Top* and *Bottom* positions, is 21.9 ± 1.6% for the F1 formulation and 22.6 ± 2.1% for the F2 formulation, in good agreement with overall aluminum concentration coming from density measurements. Considering both results from density measurements and TGA, it can be stated that F2 formulation is more homogeneous, with less gradient between *Top* and *Bottom* positions, and these findings probably imply that F1 formulation leads to more agglomeration within the printed part.

3.5. Mechanical characterization

The results of the mechanical characterization of the TPMS structures are summarized in Table 5, where the yield stress (σ_y), yield strain (ϵ_y), and Young's modulus (E) are reported. The corresponding stress–strain curves are also illustrated in Fig. 12. Three tests were performed for every structure. Table 5 shows average values of parameters of interest (ASTM D695) and then data scattering by standard deviation. Among the tested structures, the SP and the F-RD structure showed the lowest and the highest stiffness, respectively (see Table 5). Thus, E values indicate F-RD as the most suitable structure for energy absorption application [53]. In terms of σ_y, the F-RD configuration outperformed all other geometries, whereas the SP structure showed the lowest yield stress value, indicating a higher degree of ductility but reduced overall strength. Such a result is consistent with SP simple geometry and lower load bearing efficiency [54,59]. Under the tested conditions, the GY structure displayed an intermediate behavior, both in terms of stiffness and yield stress when compared to SP and F-RD.

All F1 structures demonstrated an increase in stiffness and σ_y compared to their unloaded counterparts (see Table 5 and Fig. 12). All structures exhibited an hysteresis effect during the initial phase of the compression tests, indicating energy dissipation likely associated with micro structural rearrangements, or initial geometric non linearities. Notably, the F1_F-RD specimen achieved the highest E and σ_y, confirming the reinforcing effect of the aluminum addition, while σ_y values remained relatively uniform across the structures, although the SP configuration consistently exhibited higher ductility, likely due to its more deformable cell arrangement. The addition of aluminum significantly enhanced the mechanical performance of the GY structure, resulting in a tougher and more resilient lattice structure. An increase in ϵ_y of approximately 10% was observed, indicating improved ductility, while the yield strength increased by about 30%, demonstrating a substantial

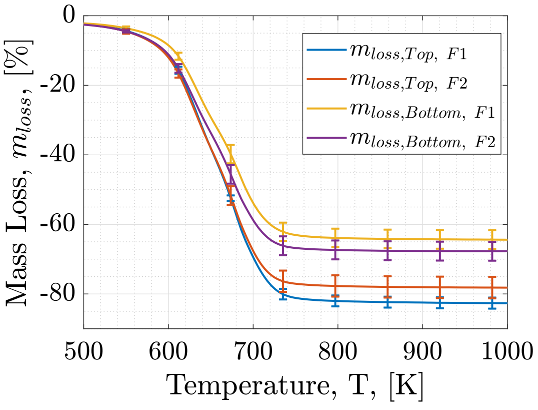

(a)

ID	Position	w_{Al} [%]
F1	Top	12.8 ± 1.6
F1	Bottom	31.0 ± 2.7
F2	Top	17.3 ± 3.1
F2	Bottom	27.8 ± 2.7

(b)

Fig. 11. TGA results: (a) TGA of samples taken from different spots and (b) localized w_{Al}.

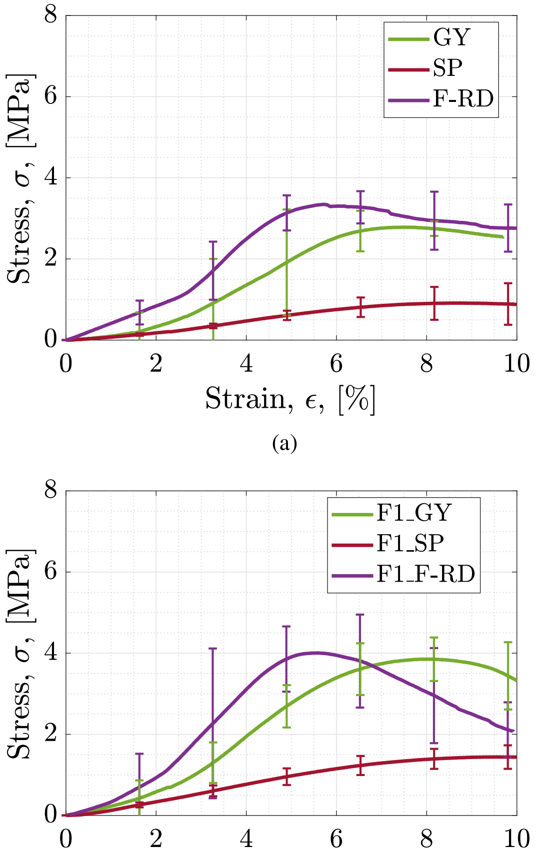

(a)

(b)

Fig. 12. Stress–strain curves comparing different TPMS geometries and the effect of powder loading: (a) unloaded formulation and (b) F1 formulation.

reinforcement effect. Under the investigated conditions, F-RD shows a relatively wider data scattering than other structures, likely due to its intrinsic higher topological complexity: aluminum addition diminished printing accuracy, making F-RD more prone to micro-fractures in its thinner regions. On the other hand, GY and SP show similar data scattering regarding loaded and unloaded specimens.

To estimate the PSD effects of Al_{III} and Al_{II}, the GY structure was chosen due to its good performance regarding ductility and toughness.

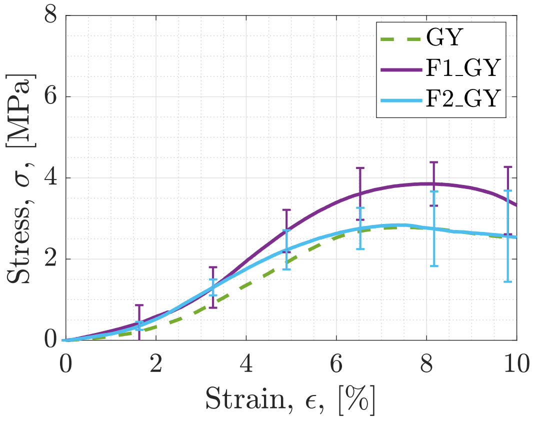

Fig. 13. Stress–strain curve for GY structure with tested formulations.

Stress–strain curve for GY structure with tested formulations is reported in Fig. 13. The formulation containing a narrower particle size distribution (F2) exhibited lower mechanical compression performance than expected (in spite of partially overlapped error-bars). While the initial response of F2_GY closely followed that of the broader particle size formulation (F1_GY), the stress–strain behavior progressively aligned more closely with the plain (unfilled) configuration (see Fig. 13). A detail of F2_GY rupture points is reported in Fig. 14. The same failure behavior is reported in every test. In contrast, F1_GY show a stochastic failure in testing. This deviation can be attributed to the reduced accuracy of the structure during printing. This behavior cannot be ascribed to either undercuring or overcuring phenomena. Typically, overcured structures exhibit higher σ_y accompanied by reduced ϵ_y, whereas undercured structures display the opposite trend [60–62].

Since the F2_GY specimen shows inferior performance compared to F1_GY in both σ_y and ϵ_y, the observed discrepancy is more likely related to microstructural defects, as could be elucidated through SEM analysis of the printed parts. SEM images of the F1_GY and F2_GY printed specimens are presented in Fig. 15. The microstructure of F2_GY reveals poorer interlayer adhesion than F1_GY, which exhibits a more homogeneous bonding between layers. In contrast, F1_GY shows agglomeration of metallic particles, as previously discussed in 3.4. Such localized particle clustering may have contributed to the enhanced mechanical response of F1_GY, where, in specific regions, the compressive behavior could be partially governed by the metal powder rather than the polymeric matrix.

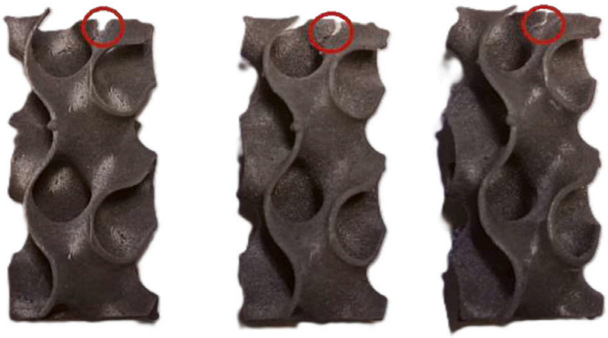

Fig. 14. F2_GY rupture point.

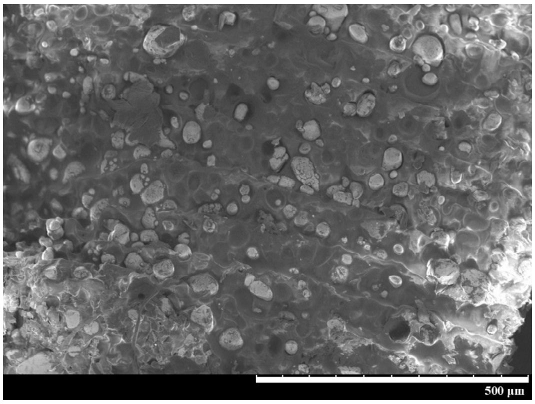

(a)

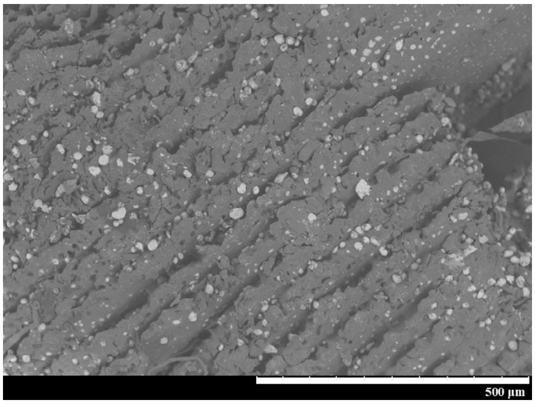

(b)

Fig. 15. SEM images of printed structure: (a) F1_GY and (b) F2_GY.

4. Conclusions

This study provides a comprehensive analysis on the printability and mechanical performance of TPMS lattice structures fabricated via DLP using photopolymer resins loaded with micron-sized air-passivated Al. The work investigates powders with particle size ($d_{3,2}$) of 29.9 μm, and 15 μm. Under the investigated conditions, surface modification of the particles emerged as key process for suspension printability. A fixed solid loading of 20 wt% (9.9 vol.%) was employed, using two different PSDs.

While the inclusion of micron-sized Al in resins do not impose significant limitations on the DLP printing di per se, the stability of the suspensions is strongly influenced by the coarse particle size. The surface modification of the powders by dispersant deposition notably reduced sedimentation rates for both Al powders. An optimal dispersant concentration of 3 wt% (relative to powder mass) was identified for both formulations, balancing suspension stability without inducing flocculation.

Working curve analysis revealed that the resin loaded with the finer Al (F2) exhibited stronger light scattering and required greater exposure energy to achieve sufficient curing.

Mechanical characterization highlighted that all TPMS structures fabricated with resin loaded with the coarser Al (F1) formulation showed enhanced mechanical performance. Improvements in both yield strength and ductility were observed, suggesting a more uniform stress distribution and reduced microstructural defects. Among the geometries tested, the GY performed better in compressive behavior, offering an effective balance between compressive strength and ductility, with ϵ_y increasing by approximately 10% and σ_y by roughly 30%. The lower mechanical behavior observed in the F2 formulation is likely linked to reduced interlayer adhesion during printing, leading to localized weaknesses and microfracture initiation under load.

Future developments of the current work should focus on (i) incorporation of other energetic materials (nanoscale, and mechanically activated powders [63]) to enhance energetic properties, (ii) optical absorbance measurements that could clarify the influence of powder absorbance on curing depth [64,65], (iii) development of purposely formulated loaded resins for enhanced printing quality and mechanical properties tailoring with low-end hardware.

CRediT authorship contribution statement

Carlo Rontini: Writing – original draft, Visualization, Validation, Resources, Investigation, Formal analysis, Data curation, Conceptualization. **Federico Giambelli:** Writing – original draft, Visualization, Validation, Investigation, Data curation, Conceptualization. **Christian Paravan:** Writing – review & editing, Visualization, Supervision, Methodology, Investigation, Formal analysis, Data curation, Conceptualization.

Funding

This research did not receive any specific grant from funding agencies in the public, commercial, or not-for-profit sectors.

Declaration of competing interest

The authors declare that they have no known competing financial interests or personal relationships that could have appeared to influence the work reported in this paper.

Acknowledgments

The authors would like to thank Ms. Letizia Calò and Mr. Davide Tamiozzo for their help in daily laboratory activities and Prof. Francesco Briatico Vangosa (Department of Chemistry, Materials and Chemical Engineering *Giulio Natta*, Politecnico di Milano) for his support with rheology analyses.

Data availability

Data will be made available on request.

References

[1] J. Sun, J. Binner, J. Bai, Effect of surface treatment on the dispersion of nano Zirconia particles in non-aqueous suspensions for stereolithography, J. Eur. Ceram. Soc. 39 (4) (2019) 1660–1667, http://dx.doi.org/10.1016/j.jeurceramsoc.2018.10.024, URL https://www.sciencedirect.com/science/article/pii/S0955221918306435.

[2] Z. Chen, J. Li, C. Liu, Y. Liu, J. Zhu, C. Lao, Preparation of high solid loading and low viscosity ceramic slurries for photopolymerization-based 3D printing, Ceram. Int. 45 (9) (2019) 11549–11557, http://dx.doi.org/10.1016/j.ceramint.2019.03.024, URL https://www.sciencedirect.com/science/article/pii/S0272884219305632.

[3] I. Kim, S. Kim, A. Andreu, J.-H. Kim, Y.-J. Yoon, Influence of dispersant concentration toward enhancing printing precision and surface quality of vat photopolymerization 3D printed ceramics, Addit. Manuf. 52 (2022) 102659, http://dx.doi.org/10.1016/j.addma.2022.102659, URL https://www.sciencedirect.com/science/article/pii/S2214860422000653.

[4] J. Feng, F. Jianzhong, X. Yao, Triply periodic minimal surface (TPMS) porous structures: From multi-scale design, precise additive manufacturing to multidisciplinary applications, Int. J. Extrem. Manuf. 4 (2022) http://dx.doi.org/10.1088/2631-7990/ac5be6.

[5] C. Wang, H. Wang, L. Tang, J. Xue, Z. Wang, H. Wei, Vat photopolymerization 3D printed SiOC-based metamaterials with triply periodic minimal surface: Microwave absorption and load-bearing properties, Addit. Manuf. 104 (2025) 104776, http://dx.doi.org/10.1016/j.addma.2025.104776, URL https://www.sciencedirect.com/science/article/pii/S221486042500140X.

[6] K. Khan, M.I. Hussain, A.K. Tareen, A. Asghar, M. Hamza, Z. Chen, Advances in vat photopolymerization 3D printing: Multifunctional materials, process innovations, and emerging applications, Mater. Sci. Eng.: R: Rep. 167 (2026) 101120, http://dx.doi.org/10.1016/j.mser.2025.101120, URL https://www.sciencedirect.com/science/article/pii/S0927796X25001986.

[7] F. Zhang, L. Zhu, Z. Li, S. Wang, J. Shi, W. Tang, N. Li, J. Yang, The recent development of vat photopolymerization: A review, Addit. Manuf. 48 (2021) 102423, http://dx.doi.org/10.1016/j.addma.2021.102423, URL https://www.sciencedirect.com/science/article/pii/S2214860421005753.

[8] D.M. Shah, J. Morris, T.A. Plaisted, A.V. Amirkhizi, C.J. Hansen, Highly filled resins for DLP-based printing of low density, high modulus materials, Addit. Manuf. 37 (2021) 101736, http://dx.doi.org/10.1016/j.addma.2020.101736, URL https://www.sciencedirect.com/science/article/pii/S2214860420311088.

[9] Q. Gu, H. Wang, W. Gao, J. Yu, X. Zhou, Preparation of large-size alumina ceramic parts by DLP 3D printing using high-solid-loading paste and optimizing the debinding process, Ceram. Int. 49 (17, Part B) (2023) 28801–28812, http://dx.doi.org/10.1016/j.ceramint.2023.06.142, URL https://www.sciencedirect.com/science/article/pii/S0272884223017297.

[10] G. Qi, H. Yao, Y. Zeng, J. Chen, Preparation and properties of highly loaded SnO2-based porous electrodes by DLP 3D printing, J. Alloys Compd. 935 (2023) 167941, http://dx.doi.org/10.1016/j.jallcom.2022.167941, URL https://www.sciencedirect.com/science/article/pii/S0925838822043328.

[11] F. Zhang, S. Zhou, H. You, G. Zhang, J. Yang, Y. Shi, 3D printing of ceramic matrix composites: Strengthening and toughening strategies, Compos. Part B: Eng. 297 (2025) 112335, http://dx.doi.org/10.1016/j.compositesb.2025.112335, URL https://www.sciencedirect.com/science/article/pii/S1359836825002252.

[12] M. Isachenkov, S. Chugunov, I. Akhatov, I. Shishkovsky, Regolith-based additive manufacturing for sustainable development of lunar infrastructure - an overview, Acta Astronaut. 180 (2021) 650–678, http://dx.doi.org/10.1016/j.actaastro.2021.01.005, URL https://www.sciencedirect.com/science/article/pii/S0094576521000060.

[13] M. Isachenkov, S. Chugunov, A. Smirnov, A. Kholodkova, I. Akhatov, I. Shishkovsky, The effect of particle size of highland and mare Lunar regolith simulants on their printability in vat polymerisation additive manufacturing, Ceram. Int. 48 (23, Part A) (2022) 34713–34719, http://dx.doi.org/10.1016/j.ceramint.2022.08.060, URL https://www.sciencedirect.com/science/article/pii/S0272884222028486.

[14] M. Isachenkov, I. Gorokh, E. Makarov, D. Verkhoturov, P. Khmelenko, N. Garzaniti, A. Golkar, Technical evaluation of additive manufacturing technologies for in-situ fabrication with Lunar regolith, Adv. Space Res. 71 (6) (2023) 2656–2668, http://dx.doi.org/10.1016/j.asr.2022.07.075, URL https://www.sciencedirect.com/science/article/pii/S0273117722007086.

[15] M. Isachenkov, A.M. Grande, G. Sala, Optimizing lunar regolith for vat polymerization and sintering: pre-processing & mineral composition impact, Ceram. Int. 50 (18, Part A) (2024) 32265–32277, http://dx.doi.org/10.1016/j.ceramint.2024.06.034, URL https://www.sciencedirect.com/science/article/pii/S0272884224024404.

[16] C. Oztan, V. Coverstone, Utilization of additive manufacturing in hybrid rocket technology: A review, Acta Astronaut. 180 (2021) 130–140, http://dx.doi.org/10.1016/j.actaastro.2020.11.024, URL https://www.sciencedirect.com/science/article/pii/S0094576520307001.

[17] D. Tkachev, Y. Dubkova, A. Zhukov, Y. Verkhoshanskiy, A. Vorozhtsov, I. Zhukov, Photocurable high-energy polymer-based materials for 3D printing, Polymers 15 (21) (2023) http://dx.doi.org/10.3390/polym15214252, URL https://www.mdpi.com/2073-4360/15/21/4252.

[18] C. Nguyen, J.C. Thomas, Performance of additively manufactured fuels for hybrid rockets, Aerospace 10 (6) (2023) http://dx.doi.org/10.3390/aerospace10060500, URL https://www.mdpi.com/2226-4310/10/6/500.

[19] Y. Chen, S. Ba, H. Ren, Additive manufacturing of a special-shaped energetic grain and its performance, Micromachines 12 (12) (2021) http://dx.doi.org/10.3390/mi12121509, URL https://www.mdpi.com/2072-666X/12/12/1509.

[20] F. Bazzal, J. Hoffmann, G. Young, M. Bortner, C. Williams, Direct ink writing of aluminized solid fuels for hybrid rockets using a dual-cure approach, ACS Appl. Eng. Mater. 3 (2025) http://dx.doi.org/10.1021/acsaenm.4c00796, URL https://pubs.acs.org/doi/10.1021/acsaenm.4c00796.

[21] R. Bisin, C. Paravan, S. Alberti, L. Galfetti, A new strategy for the reinforcement of paraffin-based fuels based on cellular structures: The armored grain - mechanical characterization, Acta Astronaut. 176 (2020) 494–509, http://dx.doi.org/10.1016/j.actaastro.2020.07.003, URL https://www.sciencedirect.com/science/article/pii/S0094576520304215.

[22] R. Bisin, C. Paravan, A new strategy for the reinforcement of paraffin-based fuels based on cellular structures: The armored grain - ballistic characterization, Acta Astronaut. 206 (2023) 284–298, http://dx.doi.org/10.1016/j.actaastro.2023.02.027, URL https://www.sciencedirect.com/science/article/pii/S0094576523000930.

[23] S. Zakeri, M. Vippola, E. Levanen, A comprehensive review of the photopolymerization of ceramic resins used in stereolithography, Addit. Manuf. 35 (2020) 101177, http://dx.doi.org/10.1016/j.addma.2020.101177, URL https://www.sciencedirect.com/science/article/pii/S2214860420305492.

[24] Y. Zhang, S. Li, Y. Zhao, W. Duan, B. Liu, T. Wang, G. Wang, Digital light processing 3D printing of AlSi10Mg powder modified by surface coating, Addit. Manuf. 39 (2021) 101897, http://dx.doi.org/10.1016/j.addma.2021.101897, URL https://www.sciencedirect.com/science/article/pii/S2214860421000622.

[25] J. Wang, J. Guo, Z. Liu, X. Cao, D. Bian, J. Cheng, S. Qian, J. Yang, Microstructure and mechanical properties of digital light processing printed AISI 316L stainless steel: Optimization of slurry and sintering process, Addit. Manuf. Front. 4 (4) (2025) 200245, http://dx.doi.org/10.1016/j.amf.2025.200245, URL https://www.sciencedirect.com/science/article/pii/S2950431725000553.

[26] D. Bian, J. Wang, J. Guo, X. Cao, S. Qian, J. Yang, W. Liu, Mechanical and tribocorrosion properties of DLP-printed AISI 316L stainless steel, Mater. Today Commun. 46 (2025) 112591, http://dx.doi.org/10.1016/j.mtcomm.2025.112591, URL https://www.sciencedirect.com/science/article/pii/S2352492825011031.

[27] L. Lin, H. Wu, Y. Li, J. Wang, S. Wu, Effect of particle size on rheology, curing kinetics, and corresponding mechanical and thermal properties of aluminum nitride (AlN) ceramic by digital light processing (DLP)-based vat photopolymerization, J. Eur. Ceram. Soc. 44 (1) (2024) 184–192, http://dx.doi.org/10.1016/j.jeurceramsoc.2023.08.048, URL https://www.sciencedirect.com/science/article/pii/S095522192300674X.

[28] E. Price, Combustion of Metalized Propellants, vol. 90, American Institute of Aeronautics and Astronautics, 1984, pp. 479–513, URL https://www.scopus.com/inward/record.uri?eid=2-s2.0-0021726905&partnerID=40&md5=702913374efbc2d2c9f33d7de5c91266.

[29] F. Maggi, S. Dossi, C. Paravan, L.T. DeLuca, M. Liljedahl, Activated aluminum powders for space propulsion, Powder Technol. 270 (2015) 46–52, http://dx.doi.org/10.1016/j.powtec.2014.09.048, URL https://www.sciencedirect.com/science/article/pii/S0032591014008481.

[30] L. Chen, W. Song, J. Lv, X. Chen, C. Xie, Research on the methods to determine metallic aluminum content in aluminum nanoparticles, Mater. Chem. Phys. 120 (2) (2010) 670–675, http://dx.doi.org/10.1016/j.matchemphys.2009.12.030, URL https://www.sciencedirect.com/science/article/pii/S0254058409007767.

[31] C. Paravan, A. Verga, F. Maggi, L. Galfetti, Accelerated ageing of micron- and nano-sized aluminum powders: Metal content, composition and non-isothermal oxidation reactivity, Acta Astronaut. 158 (2019) 397–406, http://dx.doi.org/10.1016/j.actaastro.2018.08.001, URL https://www.sciencedirect.com/science/article/pii/S0094576518303151.

[32] D. Grygier, A. Kurzawa, M. Stachowicz, K. Krawiec, M. Stepczak, M. Roszak, M. Kazimierczak, D. Aniszewska, D. Pyka, Investigations into the material characteristics of selected plastics manufactured using SLA-type additive methods, Polymers 16 (11) (2024) http://dx.doi.org/10.3390/polym16111607, URL https://www.mdpi.com/2073-4360/16/11/1607.

[33] J. Sun, J. Binner, J. Bai, 3D printing of zirconia via digital light processing: optimization of slurry and debinding process, J. Eur. Ceram. Soc. 40 (15) (2020) 5837–5844, http://dx.doi.org/10.1016/j.jeurceramsoc.2020.05.079, URL https://www.sciencedirect.com/science/article/pii/S0955221920304465.

[34] X. Xu, S. Zhou, J. Wu, C. Zhang, X. Liu, Inter-particle interactions of alumina powders in UV-curable suspensions for DLP stereolithography and its effect on rheology, solid loading, and self-leveling behavior, J. Eur. Ceram. Soc. 41 (4) (2021) 2763–2774, http://dx.doi.org/10.1016/j.jeurceramsoc.2020.12.004, URL https://www.sciencedirect.com/science/article/pii/S0955221920309730.

[35] A. Binobaid, M. De Lisi, J. Camilleri, H. Hassanin, K. Essa, Zirconia-calcium silicate bioactive composites for dental applications using DLP additive manufacturing, Bioprinting 45 (2025) e00377, http://dx.doi.org/10.1016/j.bprint.2024.e00377, URL https://www.sciencedirect.com/science/article/pii/S2405886624000496.

[36] P. Cai, L. Guo, H. Wang, J. Li, J. Li, Y. Qiu, Q. Zhang, Q. Lue, Effects of slurry mixing methods and solid loading on 3D printed silica glass parts based on DLP stereolithography, Ceram. Int. 46 (2020) http://dx.doi.org/10.1016/j.ceramint.2020.03.260, URL https://www.sciencedirect.com/science/article/pii/S0272884220309081.

[37] E. Stefan, T. Didriksen, T. Sunde, M. Fontaine, H. Ræder, P. Rørvik, Effects of powder properties on the 3D printing of BaTiO3 ceramic resins by stereolithography, Prog. Addit. Manuf. 8 (2023) 1–11, http://dx.doi.org/10.1007/s40964-023-00431-w.

[38] X. Xu, S. Zhou, J. Wu, Q. Zhang, Y. Zhang, G. Zhu, Preparation of highly dispersive solid microspherical α-Al2O3 powder with a hydrophobic surface for stereolithography-based 3D printing technology, Ceram. Int. 46 (2) (2020) 1895–1906, http://dx.doi.org/10.1016/j.ceramint.2019.09.167, URL https://www.sciencedirect.com/science/article/pii/S0272884219326987.

[39] X. Xu, S. Zhou, J. Wu, S. Liu, S. Ma, T. Cheng, Study of alumina ceramic parts fabricated via DLP stereolithography using powders with different sizes and morphologies, Int. J. Appl. Ceram. Technol. 20 (2) (2023) 1167–1193, http://dx.doi.org/10.1111/ijac.14245, arXiv:https://ceramics.onlinelibrary.wiley.com/doi/pdf/10.1111/ijac.14245.

[40] C.-J. Bae, A. Ramachandran, K. Chung, S. Park, Ceramic stereolithography: Additive manufacturing for 3D complex ceramic structures, J. Korean Ceram. Soc 54 (6) (2017) 470–477, http://dx.doi.org/10.4191/kcers.2017.54.6.12, URL http://www.jkcs.or.kr/journal/view.php?number=8079.

[41] M. Schwentenwein, J. Homa, Additive manufacturing of dense alumina ceramics, Int. J. Appl. Ceram. Technol. 12 (1) (2015) 1–7, http://dx.doi.org/10.1111/ijac.12319, URL https://ceramics.onlinelibrary.wiley.com/doi/abs/10.1111/ijac.12319.

[42] P.F. Jacobs, Rapid Prototyping & Manufacturing: Fundamentals of Stereolithography, Society of Manufacturing Engineers, 1992.

[43] M.L. Griffith, J.W. Halloran, Scattering of ultraviolet radiation in turbid suspensions, J. Appl. Phys. 81 (6) (1997) 2538–2546, http://dx.doi.org/10.1063/1.364311.

[44] S.P. Gentry, J.W. Halloran, Depth and width of cured lines in photopolymerizable ceramic suspensions, J. Eur. Ceram. Soc. 33 (10) (2013) 1981–1988, http://dx.doi.org/10.1016/j.jeurceramsoc.2013.02.033, URL https://www.sciencedirect.com/science/article/pii/S0955221913001386.

[45] S.P. Gentry, J.W. Halloran, Light scattering in absorbing ceramic suspensions: Effect on the width and depth of photopolymerized features, J. Eur. Ceram. Soc. 35 (6) (2015) 1895–1904, http://dx.doi.org/10.1016/j.jeurceramsoc.2014.12.006, URL https://www.sciencedirect.com/science/article/pii/S0955221914006633.

[46] A.D. Rakić, Algorithm for the determination of intrinsic optical constants of metal films: application to aluminum, Appl. Opt. 34 (22) (1995) 4755–4767, http://dx.doi.org/10.1364/AO.34.004755, URL https://pubmed.ncbi.nlm.nih.gov/21052313/.

[47] A.H. Schoen, Infinite Periodic Minimal Surfaces Without Self-Intersections, vol. 5541, National Aeronautics and Space Administration, 1970.

[48] M. Wohlgemuth, N. Yufa, J. Hoffman, E. Thomas, Triply periodic bicontinuous cubic microdomain morphologies by symmetries, Macromolecules 34 (2001) http://dx.doi.org/10.1021/ma0019499.

[49] D. Li, W. Liao, N. Dai, G. Dong, Y. Tang, Y.M. Xie, Optimal design and modeling of gyroid-based functionally graded cellular structures for additive manufacturing, Comput.-Aided Des. 104 (2018) 87–99, http://dx.doi.org/10.1016/j.cad.2018.06.003, URL https://www.sciencedirect.com/science/article/pii/S0010448518300381.

[50] P. Parenti, D. Puccio, B. Colosimo, Q. Semeraro, A new solution for assessing the printability of 17-4 PH gyroids produced via extrusion-based metal AM, J. Manuf. Process. 74 (2022) 557–572, http://dx.doi.org/10.1016/j.jmapro.2021.12.043, URL https://www.sciencedirect.com/science/article/pii/S1526612521009257.

[51] H. Schwarz, Gesammelte Mathematische Abhandlungen: Erster Band, Springer Berlin Heidelberg, 1890.

[52] O. Al-Ketan, R.K. Abu Al-Rub, Multifunctional mechanical metamaterials based on triply periodic minimal surface lattices, Adv. Eng. Mater. 21 (10) (2019) 1900524, http://dx.doi.org/10.1002/adem.201900524, URL https://advanced.onlinelibrary.wiley.com/doi/abs/10.1002/adem.201900524.

[53] N. Qiu, Y. Wan, Y. Shen, J. Fang, Experimental and numerical studies on mechanical properties of TPMS structures, Int. J. Mech. Sci. 261 (2024) 108657, http://dx.doi.org/10.1016/j.ijmecsci.2023.108657, URL https://www.sciencedirect.com/science/article/pii/S0020740323005593.

[54] R. Kumar, J. Ramkumar, K. Balani, Design and parametrization of TPMS lattice using computational and experimental approach, Eng. Res. Express 6 (3) (2024) 035556, http://dx.doi.org/10.1088/2631-8695/ad7109.

[55] E. Lord, A. Mackay, Periodic minimal surfaces of cubic symmetry, Current Sci. 85 (2003) 346–362.

[56] J.-Y. Lu, T. Silva, F. Alzaabi, R.K.A. Al-Rub, D.-W. Lee, Insights into acoustic properties of seven selected triply periodic minimal surfaces-based structures: A numerical study, J. Low Freq. Noise Vib. Act. Control. 43 (1) (2024) 208–219, http://dx.doi.org/10.1177/14613484231190986.

[57] K. Li, Z. Zhao, The effect of the surfactants on the formulation of UV-curable SLA alumina suspension, Ceram. Int. 43 (6) (2017) 4761–4767, http://dx.doi.org/10.1016/j.ceramint.2016.11.143, URL https://www.sciencedirect.com/science/article/pii/S0272884216321435.

[58] A. Temiz, The effect of build orientation on the mechanical properties of a variety of polymer AM-created triply periodic minimal surface structures, J. Braz. Soc. Mech. Sci. Eng. 46 (3) (2024) 121, http://dx.doi.org/10.1007/s40430-024-04709-0, URL https://link.springer.com/article/10.1007/s40430-024-04709-0.

[59] C. Zhang, Z. Jiang, L. Zhao, W. Guo, Z. Jiang, X. Li, G. Chen, Mechanical characteristics and deformation mechanism of functionally graded triply periodic minimal surface structures fabricated using stereolithography, Int. J. Mech. Sci. 208 (2021) 106679, http://dx.doi.org/10.1016/j.ijmecsci.2021.106679, URL https://www.sciencedirect.com/science/article/pii/S0020740321004100.

[60] T. Jiang, B. Guo, Y. Yu, S. Gao, B. Yan, T. Qin, Y. Xu, Y. Zhao, S. Shen, B.S. Doumbia, Effect of model exposure time on the performance of photocured digital light processing 3D printing, J. Mater. Eng. Perform. 34 (20) (2025) 23130–23137, http://dx.doi.org/10.1007/s11665-025-11030-x.

[61] R. Brighenti, L. Marsavina, M.P. Marghitas, M. Montanari, A. Spagnoli, F. Tatar, The effect of process parameters on mechanical characteristics of specimens obtained via DLP additive manufacturing technology, Mater. Today: Proc. 78 (2023) 331–336, http://dx.doi.org/10.1016/j.matpr.2023.01.092, URL https://www.sciencedirect.com/science/article/pii/S2214785323001396. 9th International Conference on Advanced Materials and Structures.

[62] J.-M. Lee, K. Son, K.-B. Lee, Optimizing printing temperature and post-curing time for enhanced mechanical property and fabrication reproducibility of 3D-printed dental photopolymer resins, Appl. Sci. 15 (21) (2025) http://dx.doi.org/10.3390/app152111552, URL https://www.mdpi.com/2076-3417/15/21/11552.

[63] C. Paravan, Nano-sized and mechanically activated composites: Perspectives for enhanced mass burning rate in aluminized solid fuels for hybrid rocket propulsion, Aerospace 6 (12) (2019) http://dx.doi.org/10.3390/aerospace6120127, URL https://www.mdpi.com/2226-4310/6/12/127.

[64] P. Sheng, G. Nie, Y. Li, L. Wang, J. Chen, X. Deng, S. Wu, Enhanced curing behavior, mechanical and thermal properties of 3D printed aluminum nitride ceramics using a powder coating strategy, Addit. Manuf. 74 (2023) 103732, http://dx.doi.org/10.1016/j.addma.2023.103732, URL https://www.sciencedirect.com/science/article/pii/S2214860423003457.

[65] Q.-W. Wang, J.-M. Wu, C. Tian, Z.-A. Shi, C.-L. Liu, X. Lin, H.-S. Xu, F. Wang, Y.-S. Shi, Preparation and properties of Si3N4 ceramics via vat photopolymerization using Si3N4 powders coated with bowl-like boehmite, Addit. Manuf. 84 (2024) 104137, http://dx.doi.org/10.1016/j.addma.2024.104137, URL https://www.sciencedirect.com/science/article/pii/S2214860424001830.